# Modified fixed-grid finite element method in shape optimization problems based on the gradientless method

**M. Heshmati**[a,*], **F. Daneshmand**[b,c] **and Y. Amini**[c]

a. *Department of Mechanical Engineering, Kermanshah University of Technology, Kermanshah, Iran.*
b. *Department of Mechanical Engineering, McGill University, Canada, H3A 2K6; Department of Bioresource Engineering, McGill University, Canada, H9X 3V9.*
c. *School of Mechanical Engineering, Shiraz University, Shiraz, Iran.*

**Abstract.** This paper presents a methodology for solving shape optimization problems where the unknown is the shape of the problem domain. The proposed algorithm is based on minimization of the stress along the design boundary calculated by the Modified Fixed Grid Finite Element Method (MFGFEM). Using MFGFEM eliminates mesh adaptation and re-meshing processes, as needed in the standard finite element method, and reduces the analysis cost significantly. In this study, a new approach for computing the stiffness matrix of boundary intersecting elements is also presented and the optimal shape of the problem domain is obtained via a simple optimization algorithm. The performance of the proposed approach is investigated for shape optimization problems. It is concluded that the results of the present method are in good agreement with other analytical and finite element solutions.

## 1. Introduction

Shape optimization problems are associated with finding the optimum profile of a component to improve the behavior of a mechanical system and minimize some properties, e.g. the weight of the body or high stress concentrations near the corners. Many investigations have been carried out and various structural optimization methods have been proposed for different optimization problems [1].

Conventional shape optimization methods are based on using the Finite Element Method (FEM) and a set of elements formed from the boundary of the problem domain. A direct relationship is then created between the problem boundary and the finite element meshes and any changes in the domain boundary will also be produced in the computational meshes. The drawback of this strategy is clear: Significant boundary changes can necessitate the adaptation or regeneration of the mesh, as it no longer provides a correct representation of the medium. Therefore, in the standard shape optimization methods based on FEM, re-meshing cannot be avoided during the optimization process if accurate analysis is to be guaranteed, especially for design problems with large changes in shape [2]. These factors incorporate a considerable amount of inefficiency in the shape optimization methods based on FEM.

An interesting approach to decrease FEM dependency on conventional mesh in shape optimization problems is to use the Fixed Grid Finite Element Method (FGFEM) [3-10] and eXtended Finite Element

*. *Corresponding author. Tel.: +98 937 3154288;*
   *Fax: +98 831 7267530*
   *E-mail address: M.Heshmati@kut.ac.ir (M. Heshmati)*

Method (XFEM) [11,12]. Both FGFEM and XFEM use a fixed non-boundary-fitted grid to perform a finite element analysis. In FGFEM, the problem domain is covered with uniform finite elements, and a homogenization technique [3] is used to compute the stiffness matrix for boundary intersecting elements. The problem domain is discretized with uniform or non-uniform finite elements in XFEM, and the step function is used to carry out integration over boundary intersecting elements [12]. It has been shown that the FGFEM and XFEM are effective in approximating the strain and stress field by their low requirements of time and computational resources. Though the above mentioned methods are equipped with excellent remesh-free properties and avoid cumbersome remeshing processes, the homogenization procedure and step function used in FGFEM and XFEM result in an inaccurate representation of the problem domain and decreases the accuracy of numerical solution [4,5,9].

The integration over discontinuous elements has already been treated by several authors and has been applied in multiphase problems [13]. In the present study, basic modifications are introduced in the original FGFEM and a new approach, called Modified FGFEM (MFGFEM), is introduced to encounter the boundary intersecting elements. The modification deals with stiffness matrix computation of boundary intersecting elements by introducing material coordinates $(r, s)$ that map the internal part of the boundary intersecting element to the rectangular or triangular master element when the internal part of the boundary element is a rectangle or triangle. A new formulation is also presented for mapping the internal part of the boundary when the internal part of the boundary intersecting element is a pentagon.

It should be noted that the stress gradient information must also be determined through a sensitivity analysis in the structural optimization problems to minimize stress concentrations [14-19]. Since the sensitivity calculation time is usually high when the number of design variables is large, a gradientless approach is used in this paper. The gradientless approaches [20-27] do not use stress derivatives for determining optimal geometries. It is well-known that the convergence rate is independent of the number of design variables in these approaches, and they are particularly appropriate for minimizing stress concentrations in shape optimization problems with a large number of design variables. The underlying strategy for these methods is to achieve a constant or nearly constant stressed design boundary by adding material where stresses are 'high' and removing it where stresses are 'low'. This strategy has been shown to be consistent with the aim of minimizing the peak stress [22-27].

In the present study, the modified fixed-grid method, based on a gradientless approach for shape optimization of components and for minimizing stress concentration, is developed to overcome drawbacks in solving shape optimization problems with FEM gradient-based methods. Cubic splines are also used in the proposed method to model the shape of the design boundary and the optimal shape of the design boundary with constant stress is achieved iteratively. The validity and performance of the method are demonstrated by solving numerical examples and comparing the results of the present analysis with those reported in the literature.

The paper is organized as follows: First, the design parameterization is described and then the notion of non-boundary fitted grids is presented. The original FGFEM is described followed by an explanation of MFGFEM. After that, the application of boundary conditions is discussed and the numerical integration of a Galerkin weak form is presented. Finally, the optimization approach is described and numerical examples are conducted. The results obtained are also compared with analytical or numerical solutions.

## 2. Design parameterization

Several methods are available in representing the boundary geometry of the structure. Most researchers use the nodal coordinates of the discrete finite element model as design variables [25,27]. However, it is not suitable for the fixed-grid solver, since node locations for the analysis remain unchanged throughout the optimization process.

Various types of parametric spline are commonly used for representing the local shape of geometric modeling. The cubic spline curves and cubic B-spline curves are as certain varieties of cubic spline function. In the cubic spline representation, the cubic spline curve is expressed in terms of the coordinates of control points and their corresponding tangents, whereas, in the B-spline [9-10] representations, the curve is represented in terms of control points of a polygon. However, when the curve passes through a set of given points, the cubic spline function, which has two continuous derivatives everywhere and possesses minimum mean curvature, is a useful representation of the design boundary. The B-spline curve is particularly useful where the curve is fitted by interactive manipulation.

In this paper, cubic spline curves are selected to represent the design boundary. Because a cubic spline is a piece-wise cubic polynomial curve that has a smooth shape, the movement of a point on the line can be controlled precisely and the control points are part of the generated curve. Waldman et al. [27] tested the suitability of using a typical cubic spline interpolation on optimal shoulder fillet shapes and found good results.

## 3. Non-boundary-fitted meshes

In the shape optimization problems based on the standard finite element method, the problem domain must be divided into a set of boundary fitted elements with predefined shapes. The elements are used for shape function construction and numerical integration. The main drawbacks of these boundary fitted elements are the difficulties that arise during the mesh generation period. Although there are many automatic mesh generation techniques, the generation of an acceptable boundary fitted mesh for bodies with a moving boundary is not a simple task.

Another strategy for the numerical solution of shape optimization problems is the use of non-boundary fitted meshes. In this strategy, it is not necessary for the elements to coincide with domain boundaries and, therefore, the boundaries can intersect the elements. The use of non-boundary-fitted meshes in the analysis of shape optimization problems reduces the mesh generation costs, because the mesh generation process is performed without considering the boundary movement. In the same way, using non-boundary-fitted meshes in the shape optimization problems reduces analysis costs significantly. A typical non-boundary-fitted mesh is shown in Figure 1. As can be seen from this figure, the intersection of elements with boundaries causes the production of elements, some portions of which are located outside the problem domain. These elements, in this paper, are called Boundary Intersecting Elements (BIE). The elements located completely inside the problem domain are named Internal Elements (IE) and the others are named External Elements (EE). The collection of IE and BIE is considered an active element set. As shown in Figure 1, the nodes are also divided into three categories: Internal Nodes (IN), External Nodes (EN), and External Boundary Nodes (EBN) which locate outside the domain boundary; this type of nodes lie on the corners of boundary intersecting elements. The collection of IN and EBN is considered an active node set.
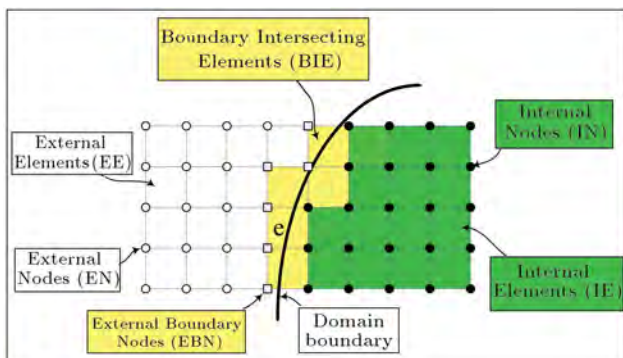


**Figure 1.** A non-boundary-fitted mesh and classification of nodes and elements.

## 4. Fixed grid finite element method

The original FGFEM uses the idea of the application of non-boundary-fitted grids in the finite element solution of the problems. In this method the homogenization technique is used for the formulation of boundary intersecting elements [3]. In the homogenization technique, it is assumed that the problem is not restricted by the original domain boundaries, and the material is distributed over the entire space with the assumption that the density and stiffness of the media is a function of space. In other words, it is assumed that the stiffness of IE is equal to the original material, but that the stiffness of EE is very low compared to the stiffness of IE. With these assumptions, the stiffness of BIE is a value between the stiffness of IE and EE corresponding to the area fraction of the internal part of BIE. In this approach, if $C_i$ is the elasticity tensor of IE, $C_e$ is the elasticity tensor of EE; the elasticity tensor of BIE is written as:

$$C_b = rC_i + (1-r)C_e, \quad r = \frac{A_i}{A}, \tag{1}$$

where $A$ and $A_i$ are the total area and area of the internal part of the BIE, respectively, and, therefore, $r$ fraction. This representation of BIE causes some inaccuracy in the formulation of BIE because only the area fraction is used for the formulation of BIE and the orientation of the boundary, with respect to the element and the shape of the internal part of the element, is not introduced in the formulation of BIE. Figure 2 shows examples of 6 different BIE which intersect the boundary in 6 different configurations. The area fraction, $r$, for all these elements is equal and, from the view point of the homogenization technique, the stiffness matrices of all these elements are the same. This causes an inaccurate representation of boundary intersecting elements.

## 5. Modified fixed grid finite element method

In this paper, some modifications on the formulation of BIE are implemented to improve the accuracy of the stiffness matrix and application of boundary conditions. The following sections explain these modifications.

### 5.1. Governing equations

Thepagebreak[3] governing equations for the static deformations of body, $\Omega$, with boundary $\Gamma$, are as



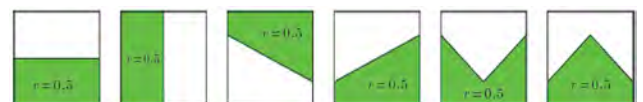**Figure 2.** Examples of different BIEs with same area fraction.

follows:

$$\nabla . \sigma + b = 0 \text{ in } \Omega, \tag{2}$$

$$u = \bar{u} \text{ on } \Gamma_u, \tag{3}$$

$$t = \sigma . n = \bar{t} \text{ on } \Gamma_t. \tag{4}$$

In these equations, $u$ is the displacement vector and $b$ is the body force. The domain boundary, $\Gamma$, is divided into two parts, $\Gamma_u$ and $\Gamma_t$, which represent the boundaries with essential and natural boundary conditions, respectively, where $\Gamma_u \cap \Gamma_t = 0$ and $\Gamma_u \cup \Gamma_t = \Gamma$. Vectors $\bar{u}$ and $\bar{t}$ are the prescribed displacements and traction forces, respectively, which are applied on the domain boundaries. $n$ is the unit outward normal vector on the boundary. The total potential energy of a continuous system can be written as follows [28]:

$$\Pi = \Pi^S - \Pi^L, \tag{5}$$

in which $\Pi^S$ is the strain energy and $\Pi^L$ is the work done by external forces. We have:

$$\Pi^S = \frac{1}{2} \int_\Omega \sigma^T \varepsilon d\Omega, \tag{6}$$

$$\Pi^L = \int_\Omega u^T b d\Omega + \int_{\Gamma_t} u^T \bar{t} d\Gamma + \sum_{i=1}^{m_l} u^T(x_i) F_t. \tag{7}$$

$F_i$ is the external concentrated force applied at point $x_i$, $m_1$ is the total number of point forces, $u$ is displacement vector, $\sigma$ is stress vector and $\varepsilon$ is strain vector. For 2D case, these values are defined as:

$$u = [u_x \ u_y]^T, \tag{8}$$

$$\sigma = [\sigma_x \ \sigma_y \ \tau_{xy}]^T, \tag{9}$$

$$\varepsilon = [\varepsilon_x \ \varepsilon_y \ \gamma_{xy}]^T. \tag{10}$$

The stress strain relation for a linear elastic material without residual stress and strains can be defined using elasticity matrix $C$ as follows:

$$\sigma = C\varepsilon. \tag{11}$$

### 5.2. Essential and natural boundary conditions

In the presented method, the penalty function method is used only for essential boundary conditions, and the natural boundary conditions are applied via numerical integration of traction forces on the boundary. In this approach, for application of essential boundary conditions, the total potential energy of the system is

modified as:

$$\Pi^\alpha = \Pi^S - \Pi^L + \frac{1}{2}\alpha_1 \int_{\Gamma_u} (u - \bar{u})^T (u - \bar{u}) d\Gamma$$

$$+ \frac{1}{2}\alpha_2 \sum_{i=1}^{m_2} (u(x_i) - \bar{u}_i)^T (u(x_i) - \bar{u}_i), \tag{12}$$

where, $\bar{u}_i$ is the prescribed displacement in the point constraint at point $x_i$, $m_2$ is the total number of point constraints and $\alpha_1$ and $\alpha_2$ are the penalty parameters. The use of a penalty function in the application of essential boundary conditions means that the rigid supports are actually replaced by a set of deformable supports, which are much stiffer than the materials used in the problem.

### 5.3. Discretization process

In this paper, a new approach for the construction of stiffness is presented. In this approach, in contrast to traditional FGFEM, the degrees of freedom of all ENs are deleted and only the degrees of freedom of INs and EBNs remain as the unknown degrees of freedom.

In this method, IEs are treated as standard finite elements with no difficulty. The strain energy of BIEs is computed using the integration of the strain energy density over the internal parts of these elements. Displacement, $u(x)$, is approximated as:

$$u(x) = N(x)U, \tag{13}$$

where $N(x)$ is the shape function matrix and $U$ is the global displacement vector. The strain vector is defined using differentiation operator $B$ as:

$$\epsilon = Bu = (\text{BN})U. \tag{14}$$

Using Eq. (14), the stress vector can be written as:

$$\sigma = C\varepsilon = C(\text{BN})U. \tag{15}$$

$\Pi^\alpha$ is then obtained by substituting Eqs. (6), (7), (13), (14) and (15) into Eq. (12) as follows:

$$\Pi^\alpha = \int_\Omega U^T (\text{BN})^T C(\text{BN}) U d\Omega \int_\Omega U^T N^T b d\Omega$$

$$- \int_{\Gamma_t} U^T N^T \bar{t} d\Gamma - \sum_{i=1}^{m_1} U^T N_i^T F_i$$

$$+ \frac{1}{2}\alpha_l \int_{\Gamma_u} (NU - \bar{u})^T (NU - \bar{u}) d\Gamma$$

$$+ \frac{1}{2}\alpha_2 \sum_{i=1}^{m_2} (N_i U - \bar{u}_i)^T (N_i U - \bar{u}_i). \tag{16}$$

It should be noted that $N_i = N(x_i)$. Using the minimum potential energy principle and differentiating Eq. (16), with respect to displacement vector $U$, we have:

$$\left[ \int_\Omega (\text{BN})^T C(\text{BN}) d\Omega + \alpha_l \int_{\Gamma_u} N^T N d\Gamma \right.$$

$$+ \alpha_2 \sum_{i=1}^{m_2} N_i^T N_i \Big] U = \left[ \int_\Omega N^T b d\Omega + \int_{\Gamma_t} N^T \bar{t} d\Gamma \right.$$

$$+ \sum_{i=1}^{m_i} N_i^T F_i + \alpha_l \int_{\Gamma_u} N^T \bar{u} d\Gamma + \alpha_2 \sum_{i=1}^{m_2} N_i^T \bar{u} \Big]. \quad (17)$$

The above equation is a set of algebraic equations that can be solved simultaneously for the unknown vector, $U$. This equation can be written as:

$$(K + K_\alpha)U = R + R_\alpha, \quad (18)$$

$$K = \int_\Omega (\text{BN})^T C(\text{BN}) d\Omega,$$

$$K_\alpha = \alpha_1 \int_\Gamma N^T N d\Gamma + \alpha_2 \sum_{i=1}^{m_2} N_i^T N_i, \quad (19)$$

$$R = \int_\Omega N^T b d\Omega + \int_{\Gamma_t} N^T \bar{t} d\Gamma + \sum_{i=1}^{m_l} N_i^T F_i,$$

$$R_\alpha = \alpha_l \int_{\Gamma_u} N^T \bar{u} d\Gamma + \alpha_2 \sum_{i=1}^{m_2} N_i^T \bar{u}. \quad (20)$$

These integrals must be numerically evaluated using nonboundary-fitted mesh. The intersection of the mesh with the domain boundary will divide the domain boundary into some boundary segments. These boundary segments are approximated by straight lines. The boundary segment of a typical boundary intersecting element ($e$), in Figure 1, is shown in Figure 3.

To improve the solution accuracy substantially, we develop a new scheme to calculate accurately the stiffness matrix of the corresponding element. To this end, we first determine the intersection points of the domain boundary and the element boundaries, e.g. points 3 and 4 in Figure 3, and connect these points to form the approximate boundary line. Note that the oblique boundary usually crosses the element domain without passing through the analysis nodes.

Now, we propose a new strategy to evaluate the stiffness. Here, we simply work with one element denoted by $e$ in Figure 1. First, we express the stiffness
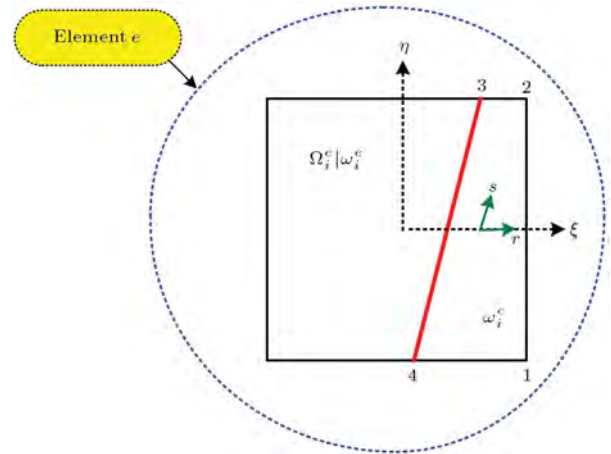


**Figure 3.** Typical boundary intersecting element with local coordinates $(\zeta, \eta)$ and material coordinate $(r, s)$.

matrix, $k^e$, as:

$$k^e = \int_{-1}^{1} \int_{-1}^{l} (\text{BN})^T(\xi, \eta) C_b \text{BN}(\xi, \eta) |J| d\xi d\eta. \quad (21)$$

where $(\xi, \eta)$ are the element local coordinates, $|J|$ is the Jacobian relating local coordinates $(\xi, \eta)$ and global coordinates, and BN denotes the matrix relating strains to nodal displacements. To integrate Eq. (21), we introduce the material coordinates $(r, s)$, which maps a normalized rectangular domain, $[-1,1]\times[-1,1]$, to the region bounded by 1-2-3-4 in Figure 3. In Figure 3, $w_i^e$ and $\Omega_i^e|\omega_i^e$ are the approximations of internal and external parts of the BIE, respectively. As in the standard bilinear finite element, the element local coordinates are expressed as:

$$\begin{pmatrix} \xi \\ \eta \end{pmatrix} = \sum_{i=1}^{4} N_i(r, s) \begin{pmatrix} \xi_i \\ \eta_i \end{pmatrix}, \quad (22)$$

where $(\xi_i, \eta_i)$ are the coordinates of points 1, 2, 3 and 4 in Figure 3 and $N_i(r, s)$ represent standard bilinear functions. If $\omega_i^e$ becomes a triangular region, it can be also treated by Eq. (22) as a degenerate case. Using the transformation (22), the element stiffness in Eq. (21) can be written as:

$$k^e = \int_{-1}^{1} \int_{-1}^{1} (\text{BN})^T(\xi, \eta) C_b \text{BN}(\xi, \eta) |J| d\xi d\eta$$

$$\approx \int_{w_i} (\text{BN})^T(\xi, \eta) C \text{BN}(\xi, \eta) |J| d\xi d\eta$$

$$= \int_{-1}^{1} \int_{-1}^{1} (\text{BN})^T(\xi(r, s),$$

$$\eta(r, s)) C \text{BN}(\xi(r, s), \eta(r, s)) |J| |\hat{J}| dr ds, \quad (23)$$

where $|\widehat{J}|$ is the Jacobian relating $(r, s)$ and $(\xi, \eta)$:

$$\widehat{J} = \begin{bmatrix} \frac{\partial \xi}{\partial r} & \frac{\partial \eta}{\partial r} \\ \frac{\partial \xi}{\partial s} & \frac{\partial \eta}{\partial s} \end{bmatrix}. \tag{24}$$

When $\Omega_i^e | \omega_i^e$ is a triangle, $\omega_i^e$ becomes a pentagon. In this case, Eq. (23) is not applicable and the stiffness matrix for the element is obtained by subtracting the stiffness of $\Omega_i^e | \omega_i^e$ from the stiffness of an internal element:

$$k^e = \int\limits_{-1}^{1} \int\limits_{-1}^{1} (\mathrm{BN})^T(\xi, \eta) C \mathrm{BN}(\xi, \eta) |J| d\xi d\eta$$

$$- \int\limits_{\Omega_i | \omega_i} (\mathrm{BN})^T(\xi, \eta) C \mathrm{BN}(\xi, \eta) |J| d\xi d\eta$$

$$= \int\limits_{-1}^{1} \int\limits_{-1}^{1} (\mathrm{BN})^T(\xi, \eta) C \mathrm{BN}(\xi, \eta) |J| d\xi d\eta$$

$$- \int\limits_{-1}^{1} \int\limits_{-1}^{1} (\mathrm{BN})^T(\xi(r, s), \eta(r, s)) C \mathrm{BN}^T(\xi(r, s),$$

$$\eta(r, s)) |J| |J^*| dr ds, \tag{25}$$

where $|J^*|$ results from the mapping between a normalized rectangle and $\Omega_i^e | \omega_i^e$.

As mentioned above, the domain integrals have been divided to integrations over IEs and BIEs. We emphasize that the stiffness evaluation above is applied only to elements lying on the boundary. For IEs, the element stiffness evaluation is exact in the proposed method. Thus, the advantages of fixed grid-based methods are the fast meshing and fast formulation of the stiffness matrix. It only requires small additional expenses to calculate the intersection points and element stiffness matrices along the boundary of the domain.

## 6. Optimization approach using splines

Figure 4 shows a plate with a fillet with a free boundary, $\Gamma$, on which there are a number of control points, $p_1, p_2, \cdots, p_k$. To achieve a boundary shape with a constant tangential stress distribution around the boundary, a number of finite element based gradientless methods have been proposed in the literature [25,29]. The underlying optimization algorithms for these methods are based on biological growth analogies, as elucidated by Heller et al. [25]. We add material where stresses are high and remove it where stresses are low. The amount of material added or removed at any point on
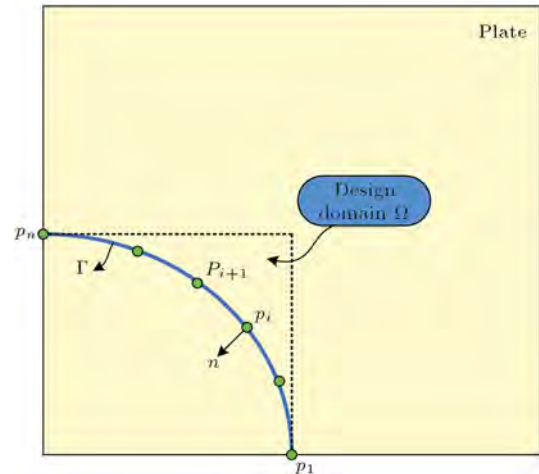
**Figure 4.** Geometry of plate with a fillet-shaped boundary.

the boundary is taken to be directly proportional to the difference between the local tangential stress and a suitable reference value. This process is then repeated iteratively until the boundary hoop stress is constant or nearly constant, within a prescribed tolerance. Hence, the amount to move a given point, $p_i$, on the design boundary (in the normal direction) is specified by the following equation [25,27,29]:

$$\delta_i = K \frac{\sigma_i - \sigma_{th}}{\sigma_{th}}, \ i = 1, 2, ..., n, \tag{26}$$

where positive $\delta_i$ indicates material addition, $\sigma_i$ is the tangential stress at $p_i$ on the boundary, $\sigma_{th}$ is the nonzero threshold boundary hoop stress, and $K$ is an arbitrary to accelerate convergence and should be determined by trial.

The selection of the threshold stress will define the type of optimization process and the initial boundary shape [25,27]. For example, if $\sigma_{th}$ is selected to be equal to the maximum (minimum) stress, only material removal (addition) will occur. However, parameter $\sigma_{th}$ is initially unknown and, hence, an arbitrary magnitude of the threshold stress has to be selected.

In this paper, for the optimization problem of minimizing the stress concentration with the prescribed design domain, a fixed point on the design boundary, $p_1$, in Figure 4 is selected. This point is fixed throughout the optimization process and its stress should converge to the uniform solution stress, finally. It should be noted that the optimization logic will become much simpler if the stress at this point is selected as $\sigma_{th}$ [29]. Here, the cubic splines, which are determined by a set of control points, $p_1, p_2, ..., p_k$, are used to define the design boundary, as shown in Figure 4. The coordinates of control points are changed by simulating biological adaptive growth and the design boundary is updated accordingly. The coordinates of a

control point are updated in the following way:

$$Y_i^{j+1}(P_i) = Y_i^j(P_i) + \delta_i^j \times d_i^j, \; i = 1, 2, ..., m, \qquad (27)$$

where $Y_i^{j+1}(P_i)$ and $Y_i^j(P_i)$ are the coordinates of control point, $P_i$, at the $(j+1)$th and $j$th iterations, respectively. $d_i^j$ is the direction of movement for $P_i$ (normal direction, $n$, in Figure 4), $m$ is the total number of control points, $\delta_i^j$ is the step of $P_i$ along the movement direction, which can be obtained by Eq. (26).

All the control points are updated sequentially using Eqs. (26) and (27), and the splines are updated accordingly. With the new shape, the stress distribution along the new design boundary will become more uniform and another modified fixed-grid finite element analysis is then undertaken. This process is repeated until the boundary tangential stress is constant or nearly constant. For such an iterative procedure, an appropriate function, RE, to monitor the solution convergence, can be written as clearly as RE approaches zero; the stresses become more uniform around the boundary:

$$\text{RE} = \left| \frac{\sigma^{\max} - \sigma^{\min}}{\sigma^{\max} + \sigma^{\min}} \right|. \qquad (28)$$

## 7. Illustrative examples

Three numerical examples are presented and discussed here to demonstrate the accuracy and power of the boundary curve approximation and proposed shape optimization method. It must be mentioned that in the first example, only the efficiency of the MFGFEM is considered and no optimization is done.

### 7.1. Infinite plate with a circular hole subject to a unidirectional load

In this example, the problem of 2D stress analysis around a circular hole in an infinite plate under unidirectional tension was examined. The schematic diagram of the problem is presented in Figure 5. This problem is essentially a two-dimensional elasticity problem and has an analytic solution. The problem was solved in plane strain condition with a circular hole in its center. Due to symmetry, only a quarter of the problem is considered. In the cutting lines, the proper boundary conditions must be applied to simulate an infinite media. Therefore, traction boundary conditions from the exact solution were applied on these lines. The analytic solution of this problem can be written in the following form [30]:

$$u = \frac{1 + \bar{v}}{\bar{E}} \sigma \left( \frac{1}{1 + \bar{v}} r \cos\theta + \frac{2}{1 + \bar{v}} \frac{a^2}{r} \cos\theta \right.$$
$$\left. + \frac{1}{2} \frac{a^2}{r} \cos 3\theta - \frac{1}{2} \frac{a^4}{r^3} \cos 3\theta \right), \qquad (29)$$
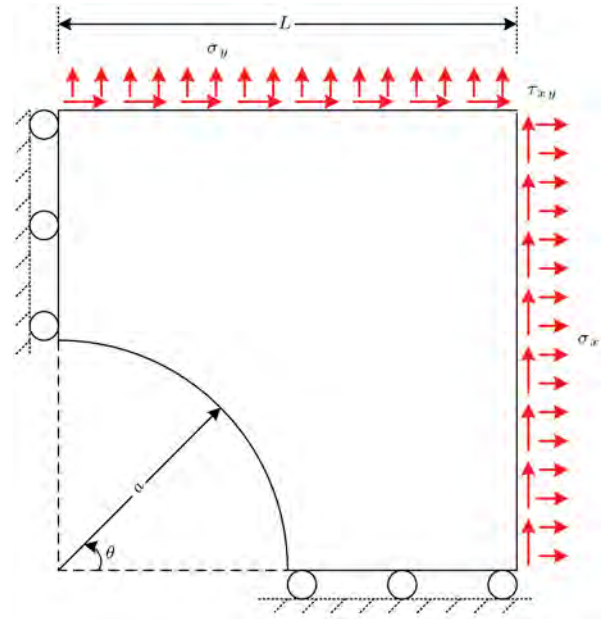


**Figure 5.** Geometry of the plate with circular hole.

$$v = \frac{1 + \bar{v}}{\bar{E}} \sigma \left( \frac{-\bar{v}}{1 + \bar{v}} r \sin\theta + \frac{1 - \bar{v}}{1 + \bar{v}} \frac{a^2}{r} \sin\theta \right.$$
$$\left. + \frac{1}{2} \frac{a^2}{r} \sin 3\theta - \frac{1}{2} \frac{a^4}{r^3} \sin 3\theta \right), \qquad (30)$$

$$\sigma_x = \sigma \left[ 1 - \frac{a^2}{r^2} \left( \frac{3}{2} \cos 2\theta + \cos 4\theta \right) + \frac{3a^4}{2r^4} \cos 4\theta \right], \qquad (31)$$

$$\sigma_y = \sigma \left[ - \frac{a^2}{r^2} \left( \frac{1}{2} \cos 2\theta + \cos 4\theta \right) + \frac{3a^4}{2r^4} \cos 4\theta \right], \qquad (32)$$

$$\tau_{xy} = \sigma \left[ - \frac{a^2}{r^2} \left( \frac{1}{2} \sin 2\theta + \sin 4\theta \right) + \frac{3a^4}{2r^4} \sin 4\theta \right]. \qquad (33)$$

The material properties are $E = 2$ GPa and $v = 2.26$. The problem is solved for 3 different grid resolutions. The first grid density consists of 16 square elements, the second grid density consists of 64 square elements and the final mesh density consists of 256 square elements. A schematic diagram of the problem domain and boundary conditions are shown in Figure 5. The relative error in energy and displacement norms is used as a measure to compare the results. The relative error in the displacement norm is calculated using the following expression:

$$d = \left( \frac{\int_\Omega (u^{ex} - u^{nu})^T (u^{ex} - u^{nu}) d\Omega}{\int_\Omega u^{ex^T} u^{ex} d\Omega} \right)^{\frac{1}{2}}, \qquad (34)$$

and the relative error in strain energy norm is calcu-

lated using:

$$e = \left( \frac{\int\limits_{\Omega} (\varepsilon^{ex} - \varepsilon^{nu})^T C (\varepsilon^{ex} - \varepsilon^{nu}) d\Omega}{\int\limits_{\Omega} \varepsilon^{ex^T} C \varepsilon^{ex} d\Omega} \right)^{\frac{1}{2}}. \qquad (35)$$

In these equations, superscripts $ex$ and $nu$ denote the exact and numeric values of the parameters, respectively. To calculate the relative errors in displacement and energy norm (Eqs. (33) and (34)), the domain integrals should be divided into integrations over IEs and internal parts of BIEs using the Gauss quadrature formula, where $u^{ex}$ and $u^{nu}$ are written as:

$$u^{ex} = \begin{bmatrix} u \\ v \end{bmatrix}, \quad u^{nu} = \begin{bmatrix} \sum\limits_{i=1}^{4} u_i^e N_i \\ \sum\limits_{i=1}^{4} v_i^e N_i \end{bmatrix}, \qquad (36)$$

where $u$ and $v$ are substituted from Eqs. (29) and (30). $u_i^e, v_i^e$ are nodal displacements of the element obtained from the present method.

The relative error norms in strain energy and displacement are presented in Figures 6 and 7 for different three type grid densities. It can be seen that the error in displacement and energy norms in MFGFEM for grid density #1 are 0.5% and 8.8%, for grid density #2 are 0.12% and 4.5%, and for the third mesh density are 0.04% and 2.3%, respectively. It is
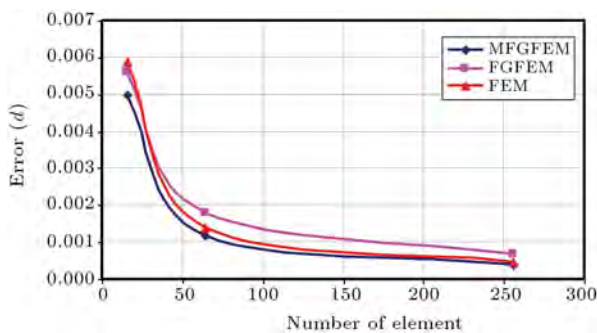


**Figure 6.** Relative error norm in displacement for different numbers of element.
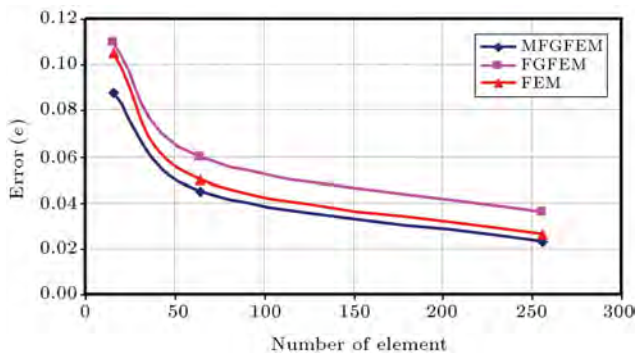


**Figure 7.** Relative error norm in strain energy for different numbers of element.

also obvious that the error norms in the present method are less than those obtained by FEM and FGFEM solvers.

## 7.2. Hole in a biaxial stress field

In this section, the benchmark structural optimization problem of a biaxial loaded plate of finite width with a hole at its center is studied. The objective of this problem is to find out the optimal hole profile to produce the minimum Von-Mises stress on the boundary of the hole. The geometry, dimensions, boundary conditions and loading of the plate are shown in Figure 8. Only a quarter of the plate has been analyzed due to symmetry. On the symmetry lines, the proper boundary conditions must be applied to simulate the complete media. A circular arc is used to define the initial design boundary and six control points are selected to parameterize the design boundary. After assuming the initial geometry, a fixed non-boundary-fitted mesh is used to solve the shape optimization of the stress concentration problem. The stress field is obtained using the MFGFEM and the parameters are then updated via a conjugate gradientless algorithm. This process is continued until achieving convergency. A typical mesh and an initial guess for the hole profile are shown in Figure 9.

To display the results, a polar coordinate system is used, in which $\theta = 0$ and $\theta = 90$ show points B and A, respectively (Figures 8 and 9). Point A is the fixed point and the stress at this point is selected as the threshold stress.

The stress far away from the concentration zone is 38.971 MPa. It is the value of stress which would exist in the plate without a hole. Therefore, this value has been taken for normalization of the results.
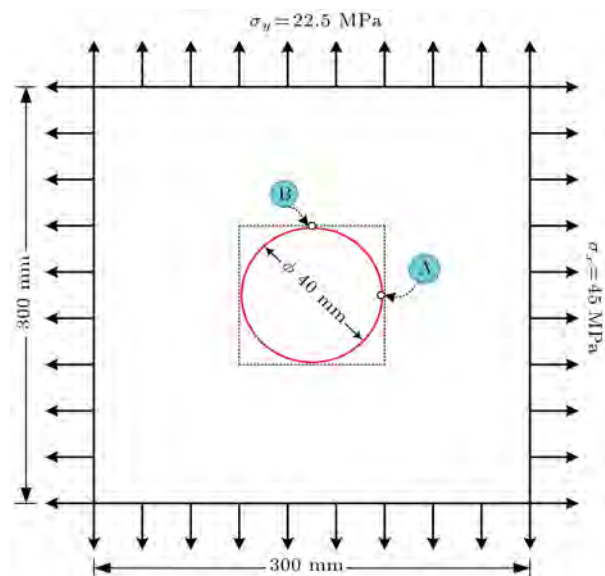


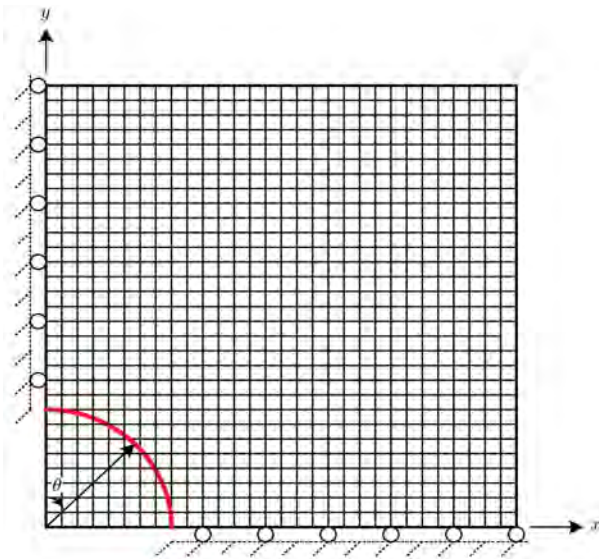**Figure 8.** Dimensions, loads and boundary conditions of the problem.

**Figure 9.** Fixed-grid mesh of one quarter of the plate with a hole.

Figure 10(a)-(c) shows the normalized Von-Mises stress contours for the initial and other iterations around the hole boundary as a function of $\theta$. The stress concentration around the initial hole is 3.2637 at $\theta = 0$ and the minimum stress is 0.51 at $\theta = 90$. It can be seen from Figure 10(a) and (b) that the convergence speed during the first iterations is considerably higher than the last iterations, because the driving force in Eq. (26) diminishes with increasing iteration. Note that the uniform von-Mises stresses appear along the hole boundary in Figure 10(c). The ratio of the major to minor axes of the resulting ellipse is 1.951, which is close to the analytical solution for the infinite plate with an ellipse, with the aspect ratio of 2:1.

The minimum possible uniform stress level along the boundary of an elliptical hole in an infinite plate is 67.5 MPa [20]. In the present results, the Von-Mises stress along the design boundary is an essentially constant level in the range 62.87-67.502 MPa, which has good agreement with the result for the infinite plate. Tekkaya and Guneri [24] investigated the same problem with the same plate geometry and boundary conditions using the biological growth method. They reported the Von-Mises stress along the design boundary is within the range 62.3- 77.9 MPa. Zhixue [29] also reported that the Von-Mises stress along the design boundary is within the range 68.98–70.30 MPa. Comparing the above results, it can be concluded that the results of the present study have extremely high accuracy.

The normalized distributions of Von-Mises stress along both the initial and final hole boundaries are shown in Figure 10(c) as a function of $\theta$. It can be noted that the stress concentration is initially 3.2637 and is reduced to 1.7404 for the optimal shape of the hole.
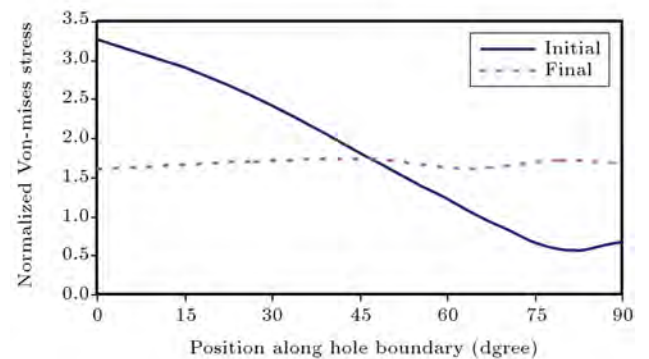
A summary of different results that are available
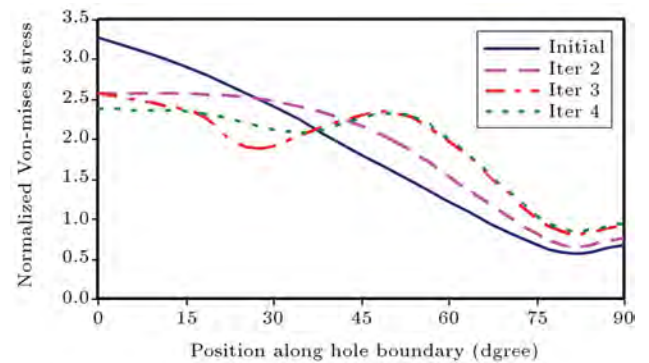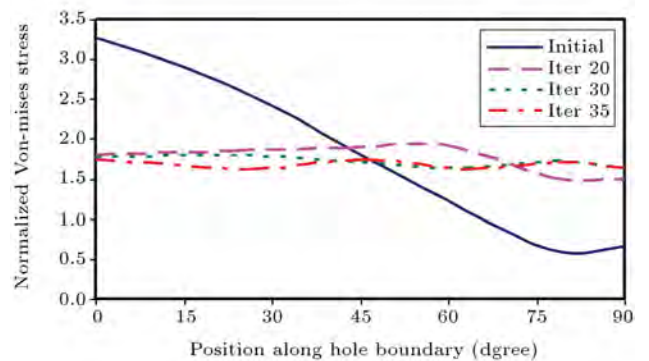


**Figure 10.** Normalized distribution of Von-Mises stress along the hole boundary.

in the literature for the same problem is presented in Table 1. The analytical solution for an infinite plate and the result of our optimization for normalized maximum Von-Mises stress around the optimal hole are given. It is shown that the present normalized maximum Von-Mises stress is lower, and there is good agreement between the present result and analytical solution.

Figure 11 shows the variation of the normalized maximum Von-Mises stress with iteration number. This result clearly shows the stability and high efficiency of the proposed optimization method. In Figure 12, the variation of boundary hole with iteration number is also shown.

**Table 1.** Comparison of published results for normalized maximum Von-Mises stress around optimal hole with the present method.

| Research | Analysis method and optimization approach | Normalized maximum Von-Mises stress around optimal hole |
|---|---|---|
| Present study | MFGFEM based on gradientless method | 1.7405 |
| Tekkaya and Guneri [20] | FEM based on biological growth method | 1.998 |
| Zhixue Wu [25] | FEM based on gradientless method | 1.804 |
| Timoshinko [26] | Analytic solution for infinite plate | 1.732 |
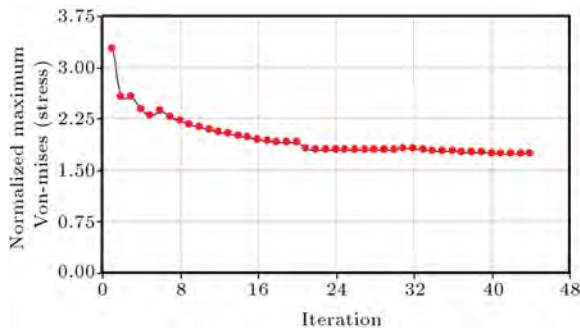


**Figure 11.** Variation of normalized maximum Von-Mises stress with iteration.
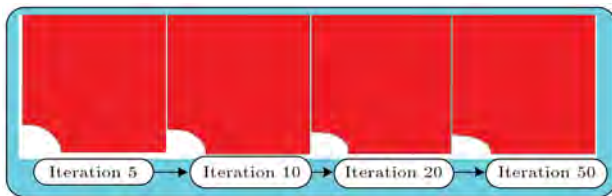


**Figure 12.** Variation of hole profile with iteration

In the following, the effect of an initial guess for the hole boundary on convergency of the uniform stress distribution along the optimal shape is considered. Thus, we assume the following curves for this purpose:

$$\left(\frac{x}{a}\right)^{\eta} + \left(\frac{y}{a}\right)^{\eta} = 1. \tag{37}$$

The above equation is plotted for different values of $\eta$ in Figure 13. It is obvious that the above equation gives a circle arc for $\eta = 2$.

The normalized maximum Von-Mises stress along the initial hole boundary for different values of $\theta$ is shown in Table 2. It is obvious that the normalized maximum Von-Mises stress decreases with increasing the value of $\eta$.

In Figure 14, the normalized distributions of the Von-Mises stress along the optimal hole boundary, as
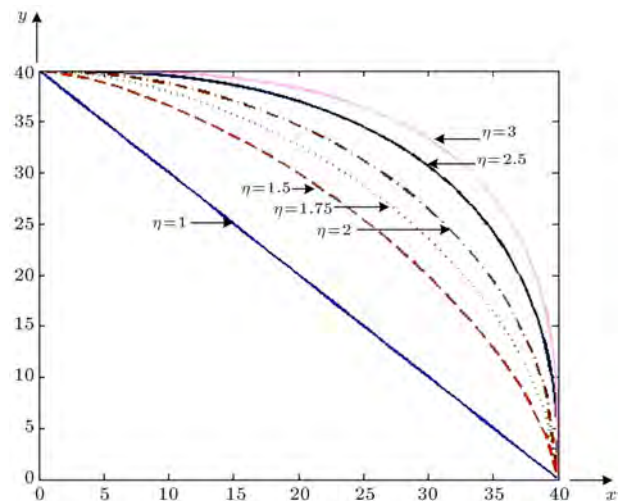


**Figure 13.** The assumed curves for initial hole profile.
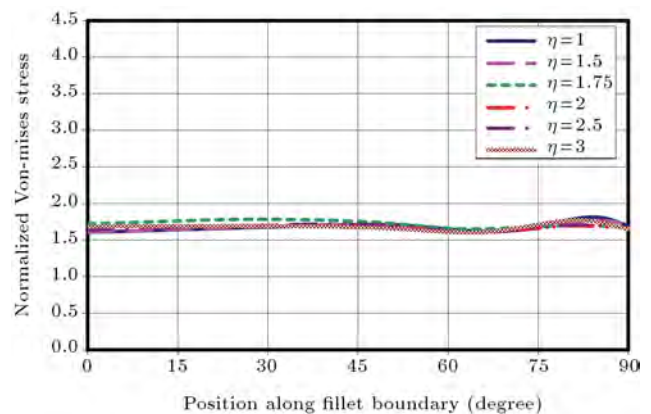


**Figure 14.** Normalized distribution of Von-Mises stress along the optimal hole boundary for different values of $\eta$.

a function of $\theta$, for different initial guesses for the hole boundary, are shown. It can be seen that for all initial guesses, the normalized stress distributions along the optimal hole boundary are the same. These results clearly show the stability and high efficiency of the optimization method.

**Table 2.** Normalized maximum Von-Mises stress around different initial hole boundaries.

| $\eta$ | 1 | 1.5 | 1.75 | 2 | 2.5 | 3 |
|---|---|---|---|---|---|---|
| Normalized maximum Von-Mises stress around initial hole | 4.2377 | 3.665 | 3.299 | 3.2637 | 2.833 | 2.686 |
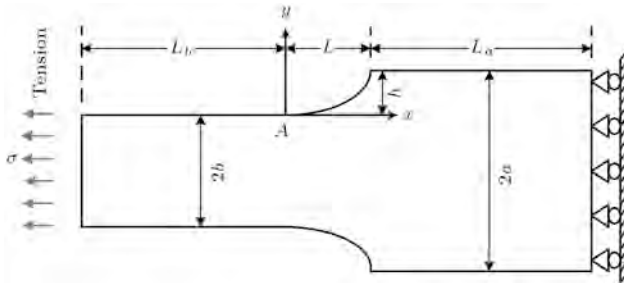


**Figure 15.** Geometry, dimension and boundary conditions of the shoulder fillet.

### 7.3. Fillet plate under tension

The general geometry and notation for a symmetric flat plate with a shoulder fillet subject to uniaxial tension is shown in Figure 15. The objective of this optimization problem is to find out the optimal fillet shape to produce the minimum stress concentration factor. Due to symmetry, only one-half of the complete plate is modeled in the MFGFE analysis. Values of $l_a = l_b = 5l$ are used to keep the effect of plate length on the state of stress in the vicinity of the fillets at a negligible level. The load is assumed to be the uniform tension of 1 MPa. A wide range of fillet geometries was optimized in order to produce useful design data. The values of $a/b = 1.33, 1.50, 1.67, 2$, and the values of $l/h = 1, 2, 3, 4, 5$ are considered in this example. A straight line is used to define the initial fillet shape. Point A is the fixed point and the stress at this point is selected as the threshold stress. The number of control points is 20.

The iteration history of the maximum principle stress is shown in Figure 16(a)-(d). These results show that the maximum principle stress converges after a few iterations.

The optimum normalized maximum principal stress values ($K_t$) obtained for all combinations of $a/b$ and $l/h$ are presented in Table 3. It can be seen that for a given $a/b$, the $K_t$ value decreases with increasing $l/h$,

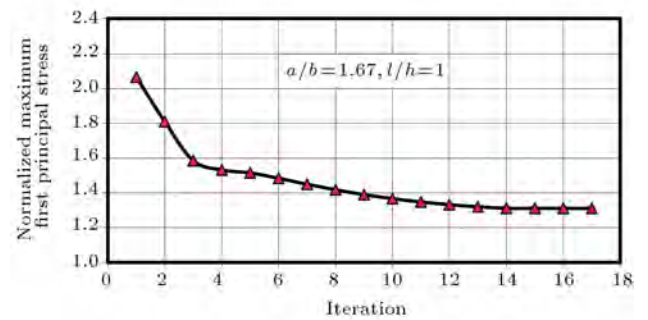**Table 3.** The optimum normalized maximum first principal stress values for different geometries.

| $l/h$ | $a/b = 1.33$ | $a/b = 1.5$ | $a/b = 1.67$ | $a/b = 2$ |
|---|---|---|---|---|
| 1 | 1.5501 | 1.4157 | 1.3481 | 1.2365 |
| 2 | 1.2545 | 1.1856 | 1.13 | 1.0591 |
| 3 | 1.1625 | 1.1023 | 1.0567 | 1.0142 |
| 4 | 1.1066 | 1.0543 | 1.0158 | 1.0047 |
| 5 | 1.0696 | 1.0238 | 1.0028 | 1 |
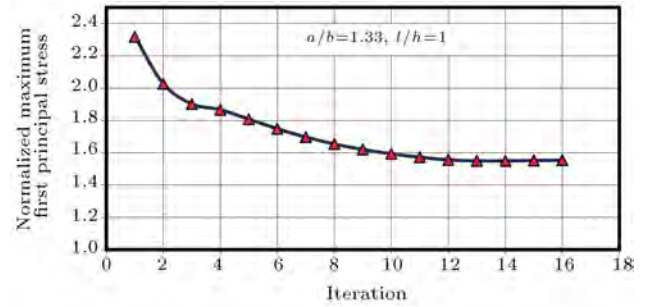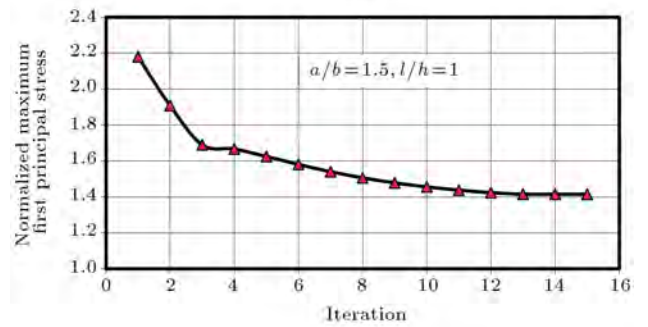


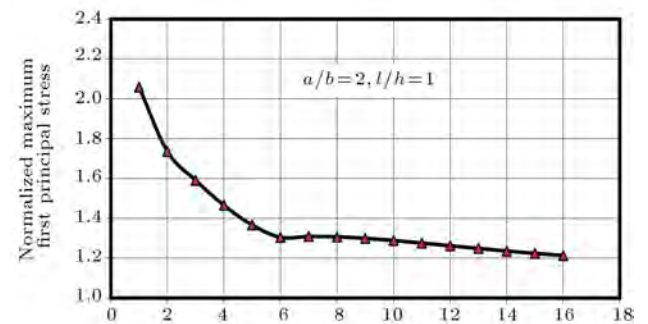**Figure 16.** Variations of maximum first principle stress with iteration number for $l/h = 1$ and $a/b = 1.33, 1.5, 1.67, 2$.

as expected. Also, for a given $l/h$, $K_t$ decreases with increasing $a/b$, which demonstrates the finite width effects. Clearly, the lowest values of $K_t$ are, therefore, obtained for cases where both $a/b$ and $l/h$ are large. It is interesting to note that in many instances, it is possible to reduce the $K_t$ values very close to unity, and a significant reduction for $K_t$ values is achieved. The normalized maximum principle stress along both the initial and optimal shoulder fillet boundaries, as a function of $x/l$, for different values of $a/b$ and $l/h = 1$, are shown in Figure 17(a)-(d). It is seen that the stresses are uniform along the full length of the optimal fillet boundary and the reduction of the maximum principal stress along the optimal fillet boundary for $a/b = 1.33$, 1.5, 1.67, 2 ($l/h = 1$) are 33.1%, 40.5%, 34.7% and 39.9%, respectively. For instance, the stresses along the optimal fillet boundary for $a/b = 1.67$ and $l/h = 1$ are in the range of 1.313-1.348, while the initial line fillet gives maximum stress, which is 34.7% higher. he optimal stress concentration factor with the present geometry is reported in the study by Waldman et al. [27] to be 1.351, which shows excellent agreement with that achieved using the present method. This comparison demonstrates that the present method can achieve good result quality in terms of accuracy and efficiency.

Non-dimensional optimal tension fillet shapes for different values of $a/b$ and $l/h$ are also shown in
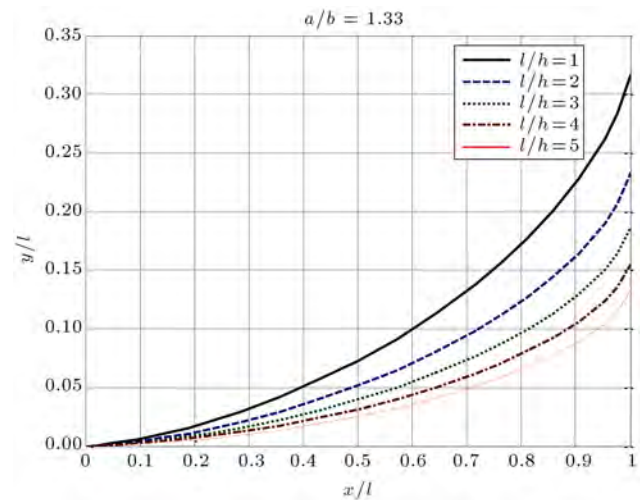


**Figure 18.** Optimal non-dimensionalised tension fillet shape for $a/b = 1.33$ and $l/h = 1, 2, 3, 4, 5$.

Figures 18-21. It is obvious that, as the fillet gets longer (i.e. $l/h$ gets larger), the optimal fillet geometry becomes flatter.

## 8. Conclusion

In this paper, a new method is developed for shape optimization problems using a modified fixed grid FEM
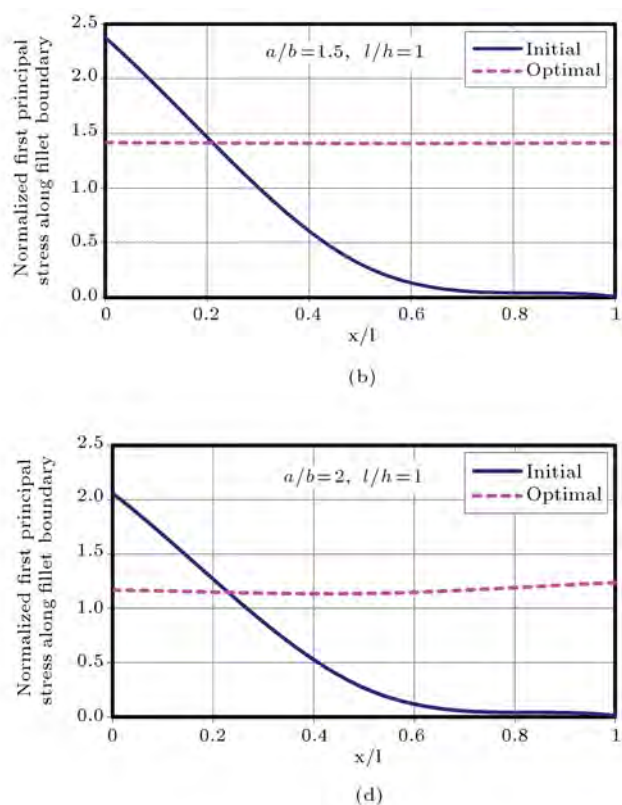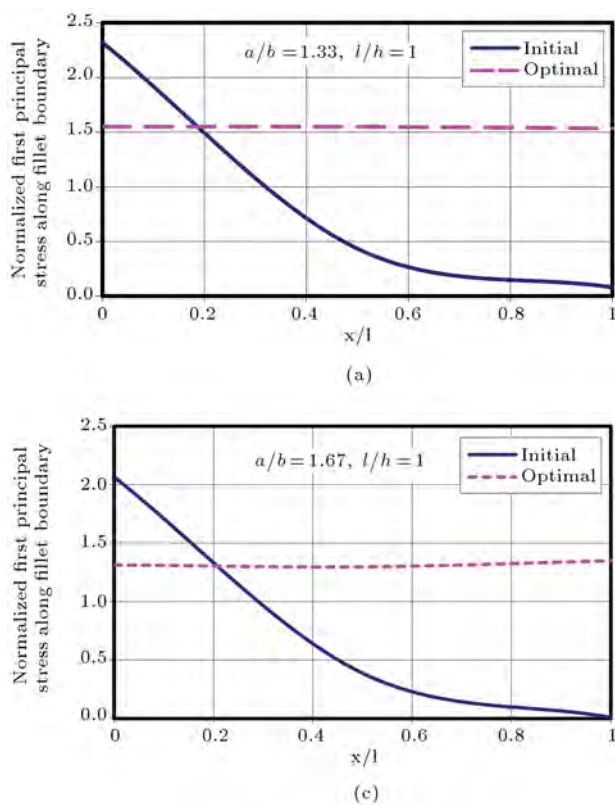


**Figure 17.** Distributions of normalized first principle stress along initial and optimal fillet boundaries as a function of $x/l$ for $l/h = 1$ and $a/b = 1.33, 1.5, 1.67, 2$.
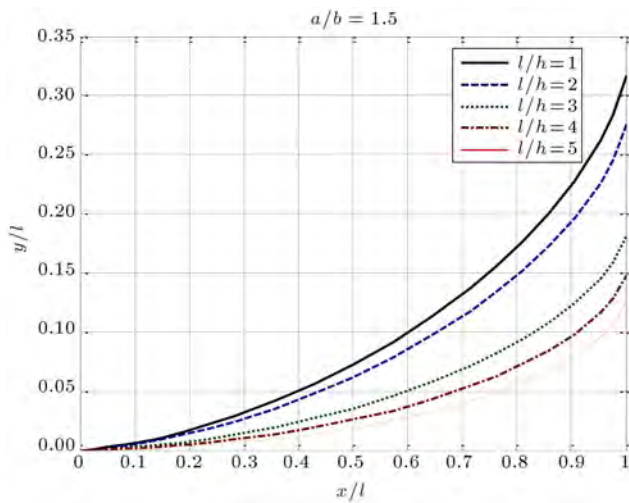
**Figure 19.** Optimal non-dimensionalised tension fillet shape for $a/b = 1.5$ and $l/h = 1, 2, 3, 4, 5$.



**Figure 21.** Optimal non-dimensionalised tension fillet shape for $a/b = 2$ and $l/h = 1, 2, 3, 4, 5$.
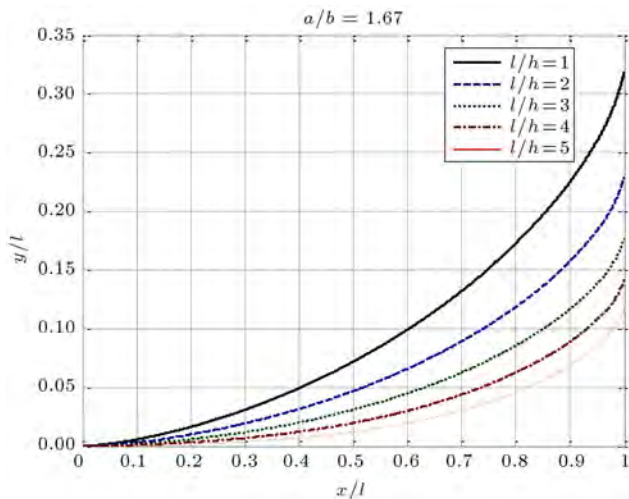


**Figure 20.** Optimal non-dimensionalised tension fillet shape for $a/b = 1.67$ and $l/h = 1, 2, 3, 4, 5$.

and a gradientless approach. The objective of the shape optimization problem is to minimize the stress concentration. A new formulation for calculating the BIEs stiffness matrix is also presented. The shape of the design boundary is modeled using cubic splines. The optimal shape of a design boundary with constant stress is achieved iteratively by adjusting the design boundary shape, based on a simple algorithm. Accurate profile shapes and associated stress concentration factors have been determined for optimal fillets in shoulder plates subjected to remote tension. A significant range of fillet geometries has been considered. The main advantage of using non-boundary-fitted meshes is to reduce the computational costs of the analysis via relaxation of the boundary conforming requirements of an acceptable mesh. This approach simplifies the preprocessing stage significantly and it is clear that preprocessing makes up a noticeable part of analysis
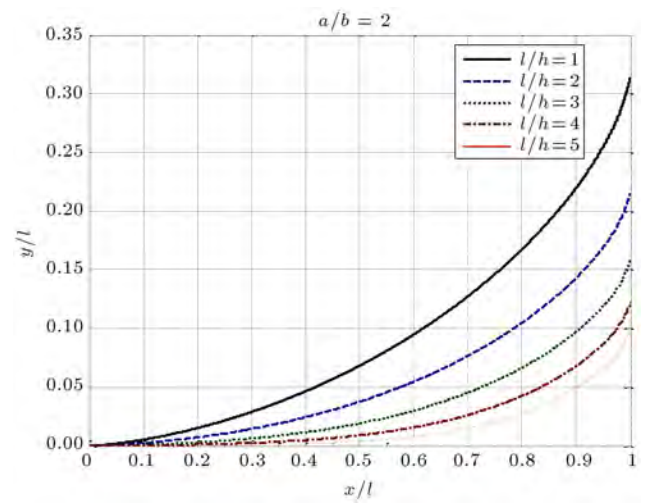
cost. The only cost that should be paid for this gain is the slight increase of effort required for evaluation of the stiffness matrix of boundary intersecting elements. Obviously, this additional effort is negligible when compared to the cost of boundary-fitted mesh generation, as in standard FEM. The accuracy and convergence of the proposed method are analyzed via numerical examples and results are compared with analytic or numerical solutions. The results show good agreement with these analytic or numerical solutions.

## References

1. Mackerle, J. "Topology and shape optimization of structures using FEM and BEM: A bibliography", *Finite Elements in Analysis and Design*, **39**, pp. 243-53 (1999-2001).

2. Bennett, J.A. and Botkin, M.E. "Structural shape optimization with geometric description and adaptive mesh refinement", *AIAA Journal*, **23**(3), pp. 458-464 (1985).

3. Bensoe, M. and Kikuchi N. "Generating optimal topologies in structural design using a homogenization method", *Computer Methods in Applied Mechanics and Engineering*, **71**, pp. 197-224 (1988).

4. Garcia, MJ. "Fixed grid finite element analysis in structural design and optimization", PhD Thesis, Aeronautical Engineering, University of Sydney, Sydney, Australia (1999a).

5. Garcia, M.J. and Steven, G.P. "Fixed grid finite elements in elasticity problems", *Engineering Computations*, **16**, pp. 145-164 (1999b).

6. Kim, H, Garcia, M.J., Querin, O.M., Steven, G.P. and Xie, Y.M. "Fixed grid finite element analysis in evolutionary structural optimization", *Engineering Computations*, **17**, pp. 427-439 (2000).

7. Woon, S.Y. Querin, O.M. and Steven, G.P. "Application of the fixed grid FEA method to step-wise GA shape optimization", In *Proceedings of Second ASMO-UK/ISSMO Conference*, Swansea, UK, pp. 265-272 (2000).

8. Garcia, M.J. and Gonzalez, C.A. "Shape optimization of continuum structures via evolution strategies and fixed grid finite element analysis", *Journal of Structural and Multidisciplinary Optimization*, **26**, pp. 92-98 (2004c).

9. Edwards, C.S, Kim, H.A. and Budd, C.J. "Smooth boundary based optimisation using fixed grid", *7th World Congress on Structural and Multidisciplinary Optimization* (2007).

10. Lee, S., Kwak, B.M. and Kim, Y. "Smooth boundary topology optimization using B-spline and hole generation", *International Journal of CAD/CAM*, **7**(1), pp. 16-31 (2007).

11. Nicolas, M. John, D. and Ted, B. "A finite element method for crack growth without remeshing", *International Journal for Numerical Methods in Engineering*, **46**(1), pp. 131-150 (1999).

12. Pierre, D., Laurent, V.M., Thibault, J. and Claude, F. "Generalized shape optimization using X-FEM and level set method", *IUTAM Symposium on Topological Design Optimization of Structures, Machines and Materials*, **137**, pp. 23-32 (2006).

13. Steven, G.P. "Internally discontinuous finite elements for moving interface problems", *International Journal for Numerical Methods in Engineering*, **18**, pp. 569-582 (1982).

14. Bletzinger, K.U., Firl, M. and Daoud, F. "Approximation of derivatives in semi analytical structural optimization", *Comput. Struct.*, **86**(13,14) pp. 1404-1416 (2008).

15. Parı́s, J., Navarrina, F., Colominas, I. and Casteleiro, M. "Stress constraints sensitivity analysis in structural topology optimization", *Comput Methods Appl. Mech. Eng.*, **199**, pp. 2110-22 (2010).

16. Chau, L., Bruns, T. and Tortorelli, D. "A gradient-based, parameter-free approach to shape optimization", *Comput. Methods Appl. Mech. Engrg.*, **200**, pp. 985-996 (2011).

17. Qi, Xia, Tielin Shi, Shiyuan Liu, Michael Yu Wang. "A level set solution to the stress-based structural shape and topology optimization", *Computers and Structures*, **90**(91), pp. 55-64 (2012).

18. Pedersen, P. and Laursen, C.L. "Design for minimum stress concentration by finite elements and linear programming", *Journal of Structural Mechanics*, **10**, pp. 243-271 (1982-1983).

19. Kaye, R. and Heller, M. "Investigation of shape optimization for the design of life extension options for an F/a-18 airframe Fs 470 bulkhead", *Journal of Strain Analysis for Engineering Design*, **35**(6), pp. 493-505 (2000).

20. Schnack, E. "An optimization procedure for stress concentrations by the finite element technique", *International Journal of Numerical Methods in Engineering*, **14**, pp. 115-124 (1979a).

21. Schnack, E. and Sporl, U. "A mechanical dynamic programming algorithm for structure optimization", *International Journal of Numerical Methods in Engineering*, **3**(11), pp. 1985-2004 (1986b).

22. Mattheck, C. and Burkhardt, S. "A new method of structural shape optimization based on biological growth", *International Journal of Fatigue*, **12**(3), pp. 185-190 (1990a).

23. Mattheck, C. and Moldenhauer, H. "An intelligent CAD method based on biological growth", *Fatigue Fracture Engng. Mater. Struct*, **13**(1), pp. 41-51 (1990b).

24. Tekkaya, A.E. and Guneri, A. "Shape optimization with the biological growth method: A parameter study", *Engineering Computations*, **13**(8), pp. 4-18 (1996).

25. Heller, M. Kaye, R. and Rose, LR. "A gradientless finite element procedure for shape optimization", *Journal of Strain Analysis for Engineering Design*, **34**(5), pp. 323-36 (1999).

26. Tran, D. and Nguyen, V. "Optimal hole profile in finite plate under uniaxial stress by finite element simulation of Durelli's photoelastic stress minimization method", *Finite Elements in Analysis and Design*, **32**, pp. 1-20 (1999).

27. Waldman, W. Heller, M. Chen, G.X. "Optimal free-form shapes for shoulder fillets in flat plates under tension and bending", *International Journal of Fatigue*, **23**, pp. 185-90 (2001).

28. Reddy, J.N., *An Introduction to the Finite Element Method*, 2nd Ed., McGraw-Hill, New York (1993).

29. Zhixue, Wu "An efficient approach for shape optimization of components", *International Journal of Mechanical Sciences*, **47**, pp. 1595-1610 (2005).

30. Timoshinko, S.P. and Goodier, J.N., *Theory of Elasticity*, 3rd Ed., McGraw-Hill, New York (1970).

## Biographies

**Mahmood Heshmati** received his BS degree in Mechanical Engineering from Razi University of Kermanshah, Iran, in 2005, and his MS degree in Mechanical Engineering from Shiraz University, Iran, in 2008. He is currently an assistant professor in Kermanshah University of Technology. His research fields include composite material, functionally graded material, nanomechanics, MEMS, NEMS, nonlocal elasticity, dynamic contact, vibrational analysis, plates and beam structures, and finite element analysis.

**Farhang Daneshmand** is Associate Adjunct Professor in the Department of Bioresource Engineering in

the Faculty of Agricultural and Environmental Sciences, and the Department of Mechanical Engineering in the Faculty of Engineering at McGill University, USA. He is also Associate Professor in the Department of Solid Mechanics in the Faculty of Mechanical Engineering at Shiraz University, Iran. His interdisciplinary experience is related to solid mechanics, including developing a fundamental understanding of nanotubes and nanoscale biological beam and shell structures, functions and behaviors including small-scale effects using nonlocal elasticity and gradient elasticity theories, linear and non-linear vibrations and the dynamic behavior of structures (inflatable structures, hydraulic structures, shell containers) with and without fluid-structure interaction, and advanced two- and three-dimensional computational solid mechanics (Isogeometric Analysis (IA), meshless methods, fixed-grid FEM).

**Yasser Amini** received BS and MS degrees in Mechanical Engineering, in 2006 and 2009, respectively, from Shiraz University, Iran, where he is currently a PhD degree student. His research interests include CFD, mesh-less methods, SPH method, fluid structure interaction, rarefied gas flow dynamics and DSMC method.